PCCP
Physical Chemistry Chemical Physics

Accepted Manuscript

This article can be cited before page numbers have been issued, to do this please use: U. E. Steiner, *Phys. Chem. Chem. Phys.*, 2026, DOI: 10.1039/D6CP00916F.

ROYAL SOCIETY OF CHEMISTRY

rsc.li/pccp

View Article Online
DOI: 10.1039/D6CP00916F

Reversible coupling of radical pair spin dynamics to a locally excited electronic singlet state

Ulrich E. Steiner

Department of Chemistry University of Konstanz, Universitätsstraße 10, 78464 Konstanz, Germany

E-Mail: ulrich.steiner@uni-konstanz.de

Abstract

Thermally assisted delayed fluorescence (TADF) in electron–donor–bridge–acceptor triads has recently been shown to provide a new way of observing the spin dynamics of charge-separated states (CSS) corresponding to linked radical pairs. In this work, we present a theoretical approach for extending standard quantum-dynamical models to describe this system. Using a representative example that combines four electronic radical-pair spin states with three nuclear spin states of a single nitrogen nucleus, we extend the Hilbert space from 12 to 15 dimensions by including the excited singlet state S_1. We derive Liouvillian operators that account for the kinetic coupling between S_1 and the CSS, including decay, charge separation, and recombination, and illustrate the resulting dynamics with numerical examples.

Introduction

Radical pairs are chemical intermediates in which weak magnetic interactions ─ significantly smaller than thermal energy at room temperature ─ with both internal and external magnetic fields can exert remarkable influence over the rates of highly exergonic chemical reactions, such as those associated with covlalent bond formation or the recombination of charge-separated states.

These effects originate from the weak splitting of four spin sublevels ─ one singlet and three triplet ─ and their associated hyperfine states, which arise from the coupling between the unpaired electron spins in the radicals and nearby magnetic nuclei. Moreover, the chemical process is governed by strict spin selection rules that require conservation of spin multiplicity between the initial radical pair and the final product state. Experimental and theoretical investigations of these and related phenomena, which now constitute the scientific field of spin chemistry,[1-7] have significantly advanced our understanding of chemical reactivity.

Historically, the first discoveries in spin chemistry were the observations of non-Boltzmann spin state populations in EPR and NMR spectra ─ phenomena attributed to chemical origins

View Article Online
DOI: 10.1039/D6CP00916F

and termed chemically induced dynamic electron polarization (CIDEP)[8-10] and chemically induced dynamic nuclear polarization (CIDNP).[11-14] Soon after, the first sizeable magnetic field effects were discovered in chemical reactions,[15, 16] a phenomenon later dubbed MARY,[17] followed by the discovery of magnetic isotope effects (MIE)[18] and by magnetic resonance exploiting magnetic field dependent reactions yields (RYDMR).[19] Magnetic field effects have also been discovered in radio luminescene, resulting from recombination fluorescence of radical ions, with oscillations indicating the coherent nature of spin processes involved.[20, 21] Insights into the underlying spin mechanisms gained from all these discoveries have proven valuable in elucidating primary electron transfer processes in photosynthesis[22-24] and have led to the hypothesis that avian magnetic navigation may be based on the radical pair mechanism ─ an idea that has inspired extensive research and continues to gain experimental support to this day.[22-30]

The energetics of a radical pair (RP) are depicted diagrammatically in Fig. 1. Depending on the multiplicity of the precursor, the RP is initially generated with either singlet or triplet electron-spin correlation. The principal energetic contributions are exchange interaction, which separates the singlet and triplet states even in the absence of an external magnetic field, and Zeeman interaction, which splits the triplet sublevels and may give rise to a condition in which one triplet substate becomes degenerate, i.e., resonant, with the singlet state. The electronic spin states are coupled through the hyperfine interaction (hfi). The isotropic, time independent component of the hfi gives rise to coherent singlet–triplet transitions, whereas the anisotropic, typically stochastically modulated hyperfine interaction (ahfi) induces relaxation. In many cases, a classical kinetic description[31, 32] that incorporates coherent processes provides an adequate representation of the observed kinetics and their magnetic-field dependence. However, such approaches are insufficient for simulating quantum beats arising from time-independent interactions such as isotropic hfi or g-factor differences between singlet and triplet substates. These effects can be observed under specific experimental conditions at early times following RP formation. Situations of this kind require a full quantum-dynamical treatment.

From an information science perspective, radical pairs (RPs) can be regarded as pairs of entangled qubits, a concept that has recently gained attention in the context of quantum information science.[33] In this framework, the maintenance and control of quantum coherence are of central importance.

View Article Online
DOI: 10.1039/D6CP00916F

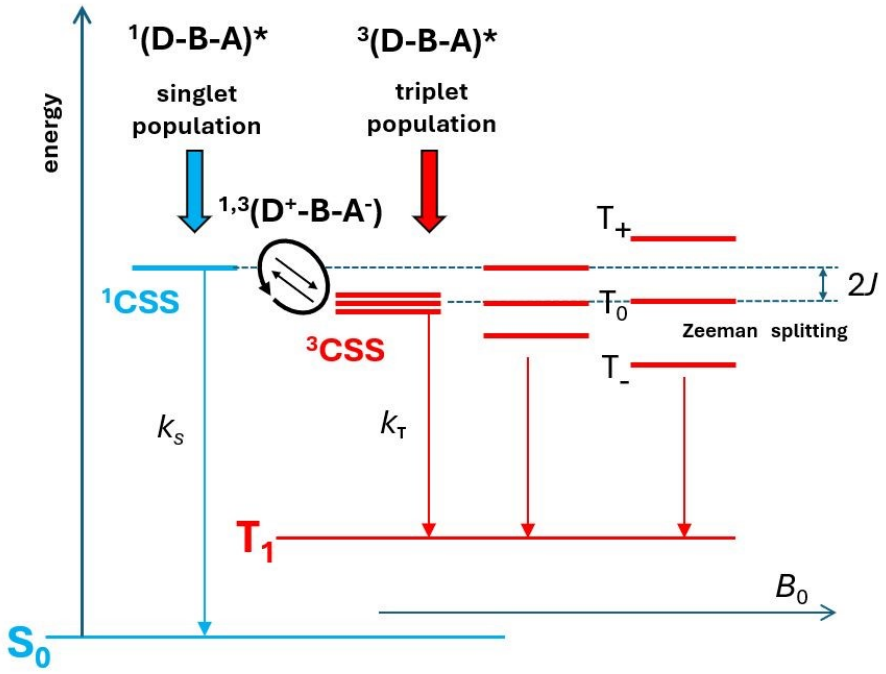

Fig. 1 Magnetic field dependent state diagram of a radical pair, here represented by a charge separated state (CSS) in an electron donor-bridge-acceptor triad showing the energetic situations between singlet and triplet substates with exchange splitting 2*J* in different magnetic fields. The circular and linear arrows represent coherent and incoherent transitions, respectively, between the different substates. The rate constants of spin selective recombination processes to singlet and triplet product states are denoted k_S and k_T for singlet and triplet, respectively.

Coherence in RPs is manifested through the observation of quantum beats, which arise from singlet–triplet (S/T) spin mixing. Although these spin substates cannot generally be distinguished spectroscopically, differences in their reaction rates toward spin-selective product channels may produce stepwise features in the overall reaction kinetics. Such effects, while difficult to detect, have been observed on the picosecond timescale under strong magnetic fields, where differences in Larmor precession frequencies ─ resulting from distinct *g*-factors of the radical partners ─ enhance S/T$_0$ transition rates.[34, 35]

Spin quantum beats are more readily accessible by spectroscopic techniques capable of distinguishing RP states of different spin multiplicities, notably electron paramagnetic resonance (EPR) spectroscopy.[36, 37] In contrast, optical detection cannot directly discriminate between RP spin states. However, following photoexcitation by a second laser pulse after initial RP formation, the enhanced reactivity of the electronically excited radicals promotes rapid conversion into products of the corresponding multiplicity. This process enables optical readout of the spin state, allowing quantum beat detection via transient optical signals.[38]

An alternative approach to differentiating RP spin states relies on singlet recombination to a fluorescent excited state, transferring singlet–triplet oscillations directly into the fluorescence signal. In non-polar solvents, radical ion pairs generated by high-energy radiation typically

View Article Online
DOI: 10.1039/D6CP00916F

possess sufficient excess energy to form locally excited singlet states upon recombination, leading to the first observations of spin quantum beats in radioluminescence.[21, 39, 40] In polar solvents, by contrast, photoexcited RPs generally lie below the energy of fluorescent locally excited singlets. A notable exception occurs with exciplex formation, which, however, requires sufficient translational and rotational mobility for the radical partners to adopt the correct mutual orientation in an exciplex.[41-45] In rigid, covalently linked donor–bridge–acceptor (D–B–A) systems, exciplex formation is typically precluded, and the nearest fluorescent singlet state remains energetically inaccessible from the RP.

Recent studies by Mani and co-workers,[46, 47] and subsequently by the Lambert group,[48] have demonstrated that structural modification of D–B–A triads can render the S_1 state energetically accessible to the charge-separated state (CSS) ─ which represents the RP in these systems. This enables the observation of delayed fluorescence arising from reverse charge recombination of the RP. The magnetic-field dependence of this delayed fluorescence provides compelling evidence identifying the RP as its precursor state. Although spin quantum beats have not yet been directly observed in thermally activated delayed fluorescence (TADF) from CSSs in D–B–A triads, these phenomena remain of significant interest. On one hand, they provide a basis for magnetic-field–sensitive imaging, and on the other, fluorescence detection offers a promising tool for single-molecule spin chemistry studies.

In this paper, we examine to what extent the TADF signal reflects the intrinsic dynamics of the CSS, and conversely, how the CSS dynamics are influenced by kinetic coupling to the S_1 state. We introduce a formal framework that integrates the reversible kinetic coupling of S_1 to the CSS with a quantum dynamical treatment of the CSS alone. This framework is then employed to address these questions through numerical model calculations.

Theoretical Basis

The stochastic Liouville equation (SLE) for the time dependent spin density matrix (DM) $\hat{\rho}(t)$ has been well established as a theoretical framework to deal with the spin and reaction dynamics of radical pairs of all kinds[3, 49, 50] including the charge separated states (CSS) we are interested in here.[32, 38, 51-57]For rigidly linked donor-bridge-acceptor triads the Liouville superoperator L

$$\frac{d\hat{\rho}(t)}{dt} = (\mathsf{L}_H + \mathsf{L}_K + \mathsf{L}_R)\hat{\rho}(t) \qquad (1)$$

View Article Online
DOI: 10.1039/D6CP00916F

comprises the following contributions

$\mathbf{L}_H$ describing the coherent spin motion due to the spin Hamiltonian $\hat{H}$

$$\mathbf{L}_H \hat{\rho} = -i([\hat{H}\hat{\rho} - \hat{\rho}\hat{H}) \tag{2}$$

$\mathbf{L}_K$ describing the stochastic decay into reaction channels selective for singlet and triplet multiplicity. The established standard form as introduced by Haberkorn[58] is

$$\mathbf{L}_K \hat{\rho} = -\frac{1}{2} k_S (\hat{Q}_S \hat{\rho} + \hat{\rho}\hat{Q}_S) - \frac{1}{2} k_T (\hat{Q}_T \hat{\rho} + \hat{\rho}\hat{Q}_T) \tag{3}$$

with $\hat{Q}_S$ and $\hat{Q}_T$ the projection operators on the electronic singlet and triplet spin substates, respectively, and k_S *and* k_T the rate constants for reaction into the pertinent reaction channels and

$\mathbf{L}_R$ describing relaxation and dephasing among the spin sublevels according to various time dependent interactions, such as anisotropies of hfc and g-tensor, electron spin-spin dipolar coupling, and fluctations of S/T splitting caused by stochastic fluctuations of rotational motion and molecular conformation. Its particular contributions will be specified in the application part below.

In solving the SLE it has become convenient to vectorize the DM by stacking the lines of the matrix into a vector, which we will denote by r. In this formalism, the Liouville superoperators are represented by square matrices applied to r. The pertinent conversion of the superoperators in eqs. (2) and (3) into the matrices L_H, L_K, and L_R is based on the general matrix relation

$$\hat{A}\hat{\rho}\hat{B} \rightarrow \hat{A} \otimes \hat{B}^{\mathrm{T}} r \tag{4}$$

where the symbol $\otimes$ denotes the Kronecker product and $\hat{B}^{\mathrm{T}}$ is the transposed matrix of $\hat{B}$.

Thereby the SLE is turned into a matrix equation

$$\frac{dr(t)}{dt} = (L_H + L_K + L_R) r(t) = L r(t) \tag{5}$$

with the general solution

$$r(t) = e^{Lt} r(0) \tag{6}$$

View Article Online
DOI: 10.1039/D6CP00916F

In the following, we consider the $4N$-dimensional Hilbert space $\mathcal{H}_{\mathrm{CSS}}$, spanned by the tensor product of a four-dimensional electronic spin space and an N-dimensional nuclear spin space. The corresponding Liouville space has dimension $(4N)^2$, and the Liouvillian superoperator is represented by a matrix $L \in \mathbb{C}^{(4N)^2\times(4N)^2}$ denoted $L_{(4N)^2\times(4N)^2}$. We then extend the Hilbert space to dimension $5N$by including the excited precursor state S_1alongside the four CSS electronic spin states. The associated Liouville space therefore has dimension $(5N)^2$, with Liouvillian matrix representation $L \in \mathbb{C}^{(5N)^2\times(5N)^2}$denoted by $L_{(5N)^2\times(5N)^2}$

For a general nuclear state defined by the nuclear quantum numbers $\{\nu_1,\nu_2,\nu_3,\ldots\nu_n\}$, with ν_i ranging from 1 to k_i the dimension *N* of the nuclear Hilbert space is given by:

$$N = \prod_{i=1}^{n} k_i \qquad (7)$$

In the present treatment, we restrict the analysis to three nuclear states arising from a ^{14}N nucleus, i.e. N = 3. Consequently, the dimensionality of the Hilbert space increases from 4×3 =12 to 5×3=15.

Subsequently, we derive the formalism for incorporating the formation of the CSS from the S_1 state with rate constant k_{CS} as well as its regeneration from the singlet substate of the CSS with rate constant k_{rCS}. It is assumed that no nuclear spin dynamics occur in the S_1 state and that the nuclear spin DM remains unchanged during both, charge separation and regeneration processes.

Incorporation of S_1 into the electronic/nuclear spin space

The state $\phi(\sigma,\nu)$ in Hilbert space represents the direct product of the electronic spin state σ in the Zeeman product basis and ν the nuclear spin state of ^{14}N, where

$$\sigma = \alpha\alpha,\alpha\beta,\beta\alpha,\beta\beta,(S_1) \qquad (8)$$

is indexed by the numbers 1-4 (5) and

$$\nu = 1,0,-1 \qquad (9)$$

is indexed by the numbers 1-3.

The ordered electronic/nuclear product states (1 -12 or 1-15 if including S_1) are

$$\alpha\alpha 1,\alpha\alpha 0,\alpha\alpha -1,\alpha\beta 1,\alpha\beta 0,\alpha\beta -1,\beta\alpha 1,\beta\alpha 0,\beta\alpha -1,\beta\beta 1,\beta\beta 0,\beta\beta -1,(S_1 1,S_1 0,S_1 -1) \quad (10)$$

The quantities $\rho_{12\times12}(\sigma,\nu;\sigma',\nu')$ or $\rho_{15\times15}(\sigma,\nu;\sigma',\nu')$ represent density operators acting on a 12- or 15-dimensional Hilbert space. The space of such operators is a 144 (225)-dimensional Liouville space. Under vectorization,

$$\rho_{12\times12}(\sigma,\nu;\sigma',\nu') \rightarrow r_{144}(i) \qquad (11)$$

where

View Article Online
DOI: 10.1039/D6CP00916F

$$i(\sigma,\nu;\sigma',\nu') = \nu' + 3(\sigma' - 1) + 4 \times 3(\nu - 1) + 3 \times 4 \times 3(\sigma - 1) \quad (12)$$

or

$$\rho_{15\times15}(\sigma,\nu;\sigma',\nu') \rightarrow r_{225}(j) \quad (13)$$

where

$$j(\sigma,\nu;\sigma',\nu') = \nu' + 3(\sigma' - 1) + 5 \times 3(\nu - 1) + 3 \times 5 \times 3(\sigma - 1) \quad (14)$$

The Liouvillian superoperators acting in the 12^2- and 15^2-dimensional Liouville spaces are represented by the matrices $L_{144\times144}$ and $L_{225\times225}$ with matrix elements defined in the Liouville basis as

$$\left(i|L_{144\times144}\,|\,j\right) \equiv L_{144\times144}(i,j) \text{ and } \left(i|L_{225\times225}\,|\,j\right) \equiv L_{225\times225}(i,j) \quad (15)$$

Equivalently, the same matrix elements may be written in their explicit Hilbert-space-index representation as

$$(\sigma,\nu;\sigma',\nu'|L_{144\times144}|\,s,n;s',n') \equiv L_{(12)^2\times(12)^2}(\sigma,\nu;\sigma',\nu'|\,s,n;s',n') \quad (16)$$

and

$$(\sigma,\nu;\sigma',\nu'|L_{225\times225}|\,s,n;s',n') \equiv L_{(15)^2\times(15)^2}(\sigma,\nu;\sigma',\nu'|\,s,n;s',n') \quad (17)$$

Here, the notation $L_{(12)^2\times(12)^2}$ and $L_{(15)^2\times(15)^2}$ emphasizes the explicit Hilbert-space-index structure of the corresponding representations. The composite Liouville-space indices $i$and $j$are obtained from the index sets $(\sigma,\nu;\sigma',\nu')$ and $(s,n;s',n')$, respectively, according to the mapping defined above for the vectorization of the density operators $r_{144}(i)$and $r_{225}(j)$.

The quantum dynamical calculation of the combined ^{1,3}CSS/S_1 system begins with the routine evaluation of the superoperator matrix for the isolated CSS system, as has been extensively documented in the literature (see also the Mathematica file in the SI).[32, 51, 54-57, 59] A detailed specification, together with representative model calculations, is provided below.

To construct the Liouville-space representation required for combining the electronic/nuclear S_1state with the CSS states, we extend the Liouvillian matrix $L_{144\times144}$ to $L_{225\times225}$. Using the index mappings defined in Eqs. (10) and (11), $L_{144\times144}$is first expressed in its explicit Hilbert-space-index representation $L_{(12)^2\times(12)^2}(\sigma,\nu;\sigma',\nu'|s,n;s',n')$. The resulting Hilbert-space-index representation is then embedded in the extended Liouvillian $L_{(15)^2\times(15)^2}$. At this stage, all matrix elements involving the electronic index 5 are set to zero. The additional S_1-related matrix elements required to describe population transfer are introduced separately below.

View Article Online
DOI: 10.1039/D6CP00916F

Thus, the present construction merely enlarges the state space and does not yet generate nuclear-spin evolution within S_1 or coherences between S_1 and the CSS states.

Finally, the extended Liouvillian is transformed back from the explicit Hilbert-space-index representation to its Liouville-space matrix representation according to Eq. (12).

$$L_{225\times225}(i(\sigma,\nu;\sigma',\nu'),j(s,n;s',n')) = L_{(15)^2\times(15)^2}(\sigma,\nu;\sigma',\nu'|s,n;s',n') \quad (18)$$

The kinetic processes to be represented are depicted in the scheme shown in Fig. 2. In the following their representation as operators in the Liouvillian are developed.

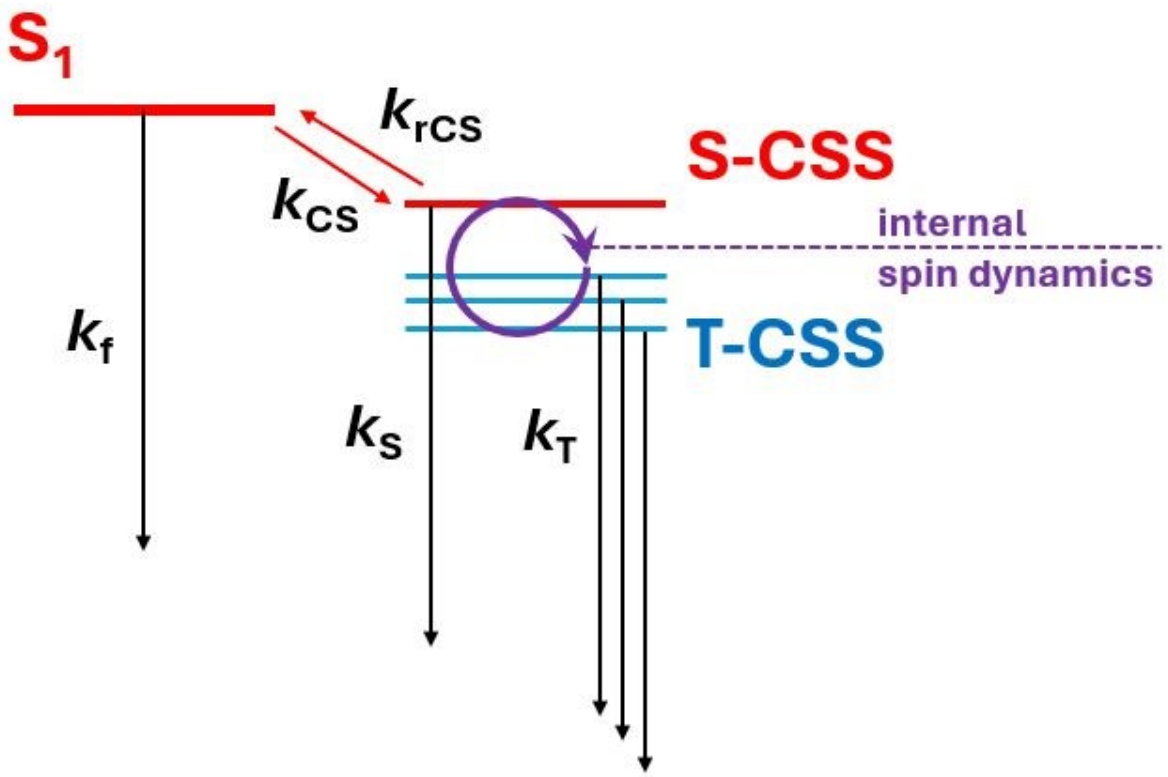

Fig. 2 Level scheme defining the stochastic rate processes: S_1-decay to ground state ("k_f" for simplicity, it encompasses also radiationless processes competing with fluorescence), S_1-transition to S-CSS (k_{CS}), regeneration of S_1 from S-CSS (k_{rCS}), S-CSS recombination to ground state (k_S), T-CSS recombination to local triplet state (k_T). Coherent and incoherent transitions among the CSS spin sublevels S-CSS and T-CSS (T_+-CSS , T_0-CSS , T_--CSS)are indicated by a circular arrow.)

Depletion kinetics of S_1

View Article Online
DOI: 10.1039/D6CP00916F

Through decay by k_f and k_{CS}, the S_1 part of the DM is diminished as follows:

$$\left(\frac{d\rho}{dt}\right)_{S_1,dep} = -(k_f + k_{CS})Q_{S_1,15}\rho Q_{S_1,15} \quad (19)$$

Here the projection operator $Q_{S_1,15}$ on the S_1 subspace is given by a 15 × 15 matrix with diagonal elements of 1 in positions 13-15 and zeros otherwise.

The DM operation given by eqn (19) is translated to the Liouvillian matrix by

$$L_{S_1,dep} = -(k_f + k_{CS})(Q_{S_1,15} \otimes Q^T_{S_1,15}) \quad (20)$$

Population of S-CSS from S_1

This contribution to the evolution of the DM (DM) is expressed as

$$\left(\frac{d\rho}{dt}\right)_{CSS,pop} = k_{CS}T_{15}P_{in}P_{ex}^T\rho P_{ex}P_{in}^T T_{15}^{-1} \quad (21)$$

Here, P_{ex} is a 15×3 projection matrix with unit elements along the diagonal positions 13 to 15 and zeros elsewhere. The operation $P_{ex}^T\rho P_{ex}$ extracts the 3×3 submatrix of ρ corresponding to the S_1 state.

Similarly, P_{in} is a 15×3 projection matrix with unit elements along the diagonal positions 7 to 9 and zeros otherwise. The transformation $P_{in}P_{ex}^T\rho P_{ex}P_{in}^T$ therefore inserts the extracted 3×3 submatrix representing the S_1 state into the position corresponding to the ^{1}CSS state within the coupled-basis representation of ρ. Finally, the transformation matrix T_{15} converts the resulting matrix representation into the Zeeman basis. The matrix transformation given by eqn (21) translates to the Liouville space as

$$L_{CSS,CS} = k_{CS}(T_{15}P_{in}P_{ex}^T) \otimes (P_{ex}P_{in}^T T_{15}^{-1})^T \quad (22)$$

Effect of reverse charge separation on the density matrix (DM)

The effect of reverse charge separation (rCS) on the DM is expressed within the Haberkorn convention (cf. eqn (3)) as

$$\left(\frac{d\rho}{dt}\right)_{CSS,rCS} = -\frac{1}{2}k_{rCS}(Q_{1CSS,15}\rho + \rho Q_{1CSS,15}) \quad (23)$$

View Article Online
DOI: 10.1039/D6CP00916F

which corresponds to the Liouville space operator

$$L_{CSS,rCS} = -\frac{1}{2}k_{rCS}(Q_{1CSS,15} \otimes U_{15} + U_{15} \otimes Q_{1CSS,15}) \quad (24)$$

Here $Q_{^1CSS,15}$ denotes the projection operator onto the ^{1}CSS spin substate and U_{15} denotes the 15×15 unit matrix.

Repopulation of S_1 by reverse charge separation from CSS

The corresponding time dependence of the DM due to the repopulation of the S_1state via reverse charge separation is given by

$$\left(\frac{d\rho}{dt}\right)_{S_1,rCS} = k_{rCS}(Q_{in}Q_{ex}^T T_{15}^{-1}\rho T_{15} Q_{ex}Q_{in}^T) \quad (25)$$

where $Q_{in} = P_{ex}$ and $Q_{ex} = Q_{in}^T = P_{in}^T$ are projection operators related to P_{ex} and P_{in}. The combined operation of these matrices, when applied to the DM in the coupled basis $T_{15}^{-1}\rho T_{15}$ yields the required contribution to the S_1 submatrix.

The corresponding Liouville-space operator is then given by

$$L_{S_1,rCS} = k_{rCS}(Q_{in}Q_{ex}^T T_{15}^{-1}) \otimes (T_{15}Q_{ex}Q_{in}^T)^T \quad (26)$$

Finally, the complete Liouville operator, required for obtaining the time-dependent solution of the DM according to eqn (6), can be expressed as

$$L = L_{225\times225} + L_{S_1,CS} + L_{CSS,CS} + L_{CSS,rCS} + L_{S_1,rCS} \quad (27)$$

View Article Online
DOI: 10.1039/D6CP00916F

Numerical Applications

Parametrization

The various components of the Liouvillian in eqn (5) will be parametrized as follows:

Hamiltonian

Besides Zeeman interaction with equal g-factors g_e of the two radicals, and exchange interaction *J,* we take into account isotropic hyperfine coupling with only one nitrogen atom specified by $\boldsymbol{a_N}$. Thus

$$\hat{H} = a_N(\hat{I}_{N,x}\hat{S}_{1,x} + \hat{I}_{N,y}\hat{S}_{1,y} + \hat{I}_{N,z}\hat{S}_{1,z}) + \omega_0(\hat{S}_{1,z} + \hat{S}_{2,z}) - 2J(\hat{S}_{1,x}\hat{S}_{2,x} + \hat{S}_{1,y}\hat{S}_{2,y} + \hat{S}_{1,z}\hat{S}_{2,z}) \quad (28)$$

where $\hat{S}_{i,x},\hat{S}_{i,y},\hat{S}_{i,z}$ and $\hat{I}_{N,x},\hat{I}_{N,y},\hat{I}_{N,z}$ denote the components of the respective spin operators and $\omega_0 = \gamma_e B_0$is the Larmor frequency.

Reaction Operator

The form of the reaction operator has been given in eqn (3), the parameters k_S and k_T denoting the specific reaction constants for singlet and triplet recombination.

Relaxation Operator

The relaxation operator involves the effect of anisotropic hyperfine interaction at the nitrogen center with a coupling constant ΔA and the rotational correlation time τ_c. The Nakashima-Zwanzig formalism as descibed by Fay et al.[60] was applied. Since the reaction constant k_S can compensate for general, field independent relaxation, we did not include the such a contribuition explicitly in our calculations here.
Furthermore S/T dephasing is taken into account by the super operator matrix

$$L_{STD} = -k_{STD}(\hat{Q}_S \otimes \hat{Q}_T + \hat{Q}_T \otimes \hat{Q}_S) \quad (29)$$

where $\hat{Q}_S$and $\hat{Q}_T$are the projection operators on singlet and triplet CSS in Hilbert space, and k_{STD} is the singlet/triplet dephasing rate constant.

In the following we will apply the general formalism to calculate the S_1-coupled CSS dynamics for two typical scenarios, where the CSS evolution in the absence of S_1-coupling is

a) is purely coherent
b) follows a realistic scenario, recently observed in an experimental case

View Article Online
DOI: 10.1039/D6CP00916F

Purely coherent spin evolution

The parameter set for this case was taken as follows (time units are in ns):

Table 1 Parameter values for coherent spin evolution (time units: ns)

k_{CS}	k_{rCS}	k_f	k_S	k_T	k_{STD}	$2J$	ΔA,mT	a, mT
1	0.025	0.25	0	0	0	0	0	1.0

In case of decoupling from S_1 it leaves the RP evolution completely coherent, with no decay and relaxation. The values of the rate constants involving S_1 represent efficient coupling to the CSS. In Fig. 3 the time dependences of the populations of several states of interest are shown. In all cases, the CSS state oscillates between S-CSS and T-CSS with an angular frequency of 3/2 a = 0.264 at zero field and of a = 0.166 at high field. These frequencies correspond to the energetic splittings at the pertinent fields. The delayed fluorescence represented by the population of S_1 oscillates in phase with the S-CSS population with about equal depth of modulation.

As shown in the SI (cf. Section S1), the uncoupled CSS does not decay, which is trivial for $k_S = k_T = 0$, and the oscillations are free of damping. Thus it can be concluded that under kinetic coupling conditions it is the process of reverse CS that causes the damping of the oscillations in the CS-state. In the literature[58, 61] it has been shown that spin-selective reaction described by the Haberkorn approach causes dephasing by a rate constant of ½ k_{ssel}, if k_{ssel} is the rate constant of the spin-selective reaction. One should note, however, that this result has been obtained under restricted conditions (e.g. S, T_0) model system. In the present case, with k_{rCS} as the rate constant of the spin-selective process, and consideration of the full four spin-state system (S, T_+,T_0, T_-) the associated dephasing rate constant is ¼ k_{rCS} corresponding to a value of 0.025 /4 = 0.00625 in the above example. Although this aspect has not been further investigated, we note that for a purely electronic 5-state system comprising the 4 CSS spin states and the kinetically coupled S_1 state, with coherent oscillations driven by the exchange interaction, the rate constant of dephasing (decoherence) has been found to vary between k_{rCS} /2 and k_{rCS}/4.

View Article Online
DOI: 10.1039/D6CP00916F

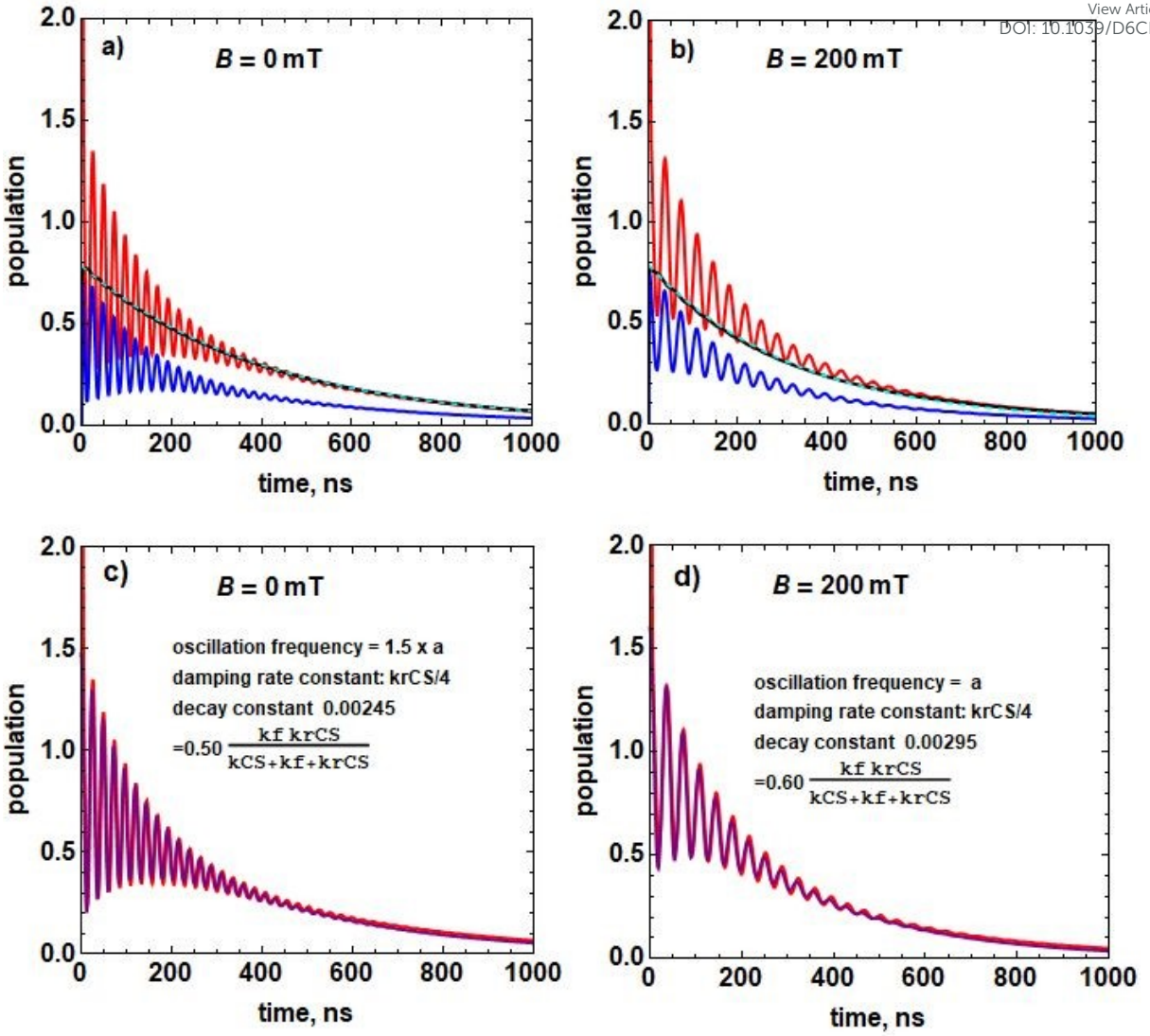

Fig. 3 Time evolution under conditions of coherent spin evolution (Table 1). Populations of S_1(x 100, red), total CSS (black), cyan: exponential simulation, S-CSS in S_1-coupled CSS (blue), a) and c) at zero field, b) and d) at 200 mT. c) and d) show the simulations of S_1 decay including the simulation of their oscillations and their damping (purple).

Regarding the decay time of delayed fluorescence we refer to the classical rate description (cf. eq. (30), Here the symbol ^{3}LE refers to a locally excited triplet state) described in the parallel paper.[48]

$$S_0 \xleftarrow{k_f} S_1 \underset{k_{rCS}}{\overset{k_{CS}}{\rightleftarrows}} \mathrm{CS} \xrightarrow{k_{CSS}} (\mathrm{S_0}, {}^3\mathrm{LE}) \qquad (30)$$

In that simplified picture, the internal spin dynamics of the CS-state is not considered explicitly, but a stationary ratio of the four spin substates is assumed with a concomitant global decay constant k_{CSS}. The following relation has been derived for the slow component (delayed fluorescence) of S_1 decay.

$$k_{\mathrm{slow}} = \tfrac{1}{2}(k_f + k_{\mathrm{CS}} + k_{\mathrm{rCS}} + k_{\mathrm{CSS}} - \sqrt{(k_f + k_{\mathrm{CS}} + k_{\mathrm{rCS}} + k_{\mathrm{CSS}})^2 - 4(k_f k_{\mathrm{CSS}} + k_{\mathrm{CS}} k_{\mathrm{CSS}} + k_f k_{\mathrm{rCS}})}) \qquad (31)$$

View Article Online
DOI: 10.1039/D6CP00916F

In the limit of slow k_{CSS} it is approximated by

$$k_{\mathrm{slow},0} = \frac{k_f k_{rCS}}{k_f + k_{\mathrm{CS}} + k_{rCS}} \quad (32)$$

For the parameter values of the present example rate constants of 0.00245 and 0.00295 have been obtained in zero field and high field, respectively. A value of 0.0049 is obtained for $k_{slow,0}$ by eqn (32). In the simple model, however, the rate constant is not spin-dependent. Produced from S_1, the CSS always remains in the S-CSS substate. Taking into account the decrease of the average singlet character of the CSS under conditions of full spin dynamics, it is qualitatively clear that the actual recombination rate must be reduced. As shown in the SI (cf. Section S2) the reduction factors of 0.50 and 0.60 for zero field and high field, respectively, can be rationalized by the average singlet character of the CSS.

As shown in Fig. 3, the population of S_1, and thus the delayed fluorescence intensity, closely follows the population of the singlet component of the S-CSS, accurately reproducing its oscillation period, damping, and overall decay. On the other hand, Fig. S1 demonstrates that kinetic coupling between the CSS and S_1 modifies the decay behavior of the unperturbed CSS and further damps any oscillations peculiar to the CSS spin dynamics, with the rate constants k_{f}, k_{CS} and k_{rCS} exerting distinct influences. These effects are analyzed and rationalized in detail in Section S5 of the Supporting Information. In addition to the features illustrated in Fig. 3, Fig. S6 highlights a further effect, namely a phase shift between the oscillations of the S_1 and S-CSS populations. This phase shift is governed primarily by the sum of the rate constants, $k_{\mathrm{CS}} + k_{\mathrm{rCS}}$.

In principle, quantum beats can be observed in radical pairs when the spin dynamics are dominated by a small number of hyperfine couplings or by the Δg mechanism, the latter typically requiring high magnetic fields. If these conditions are satisfied for an isolated CSS state, the reversible kinetic coupling to the S_1 state, which is a prerequisite for TADF, does not in itself suppress the oscillations, provided that the associated rate constant k_{rCS} does not lead to efficient decoherence according to the criterion given in Eq. (28).

To illustrate this point, we have added to the Supporting Inormation (cf. Section S4) a simulation of a CSS state previously shown to exhibit quantum beats[38] under a hypothetical reversible kinetic coupling to the S_1 state using the parameter values listed in Table 2. The simulations demonstrate that pronounced TADF quantum beats would still be observed.

Thus, if quantum beats are present in the isolated CSS, their observability by TADF depends on whether the reversible kinetic coupling to the S_1 state remains sufficiently slow to preserve that coherence.

View Article Online
DOI: 10.1039/D6CP00916F

More general parametrization

Secondly, we investigate a more general parametrization, loosely adapted to parameters corresponding to the experimentally studied triad **(Cl)TAA–mB–PDI** in Ref.[48].

Table 2 Generic set of parameters (time units: ns)

k_{CS}	k_{rCS}	k_f	k_S	k_T	k_{STD}	τ	$2J$, mT	ΔA,mT	a, mT
1	0.025	0.25	0.001	0.02	0.1	0.6	10	1.5	1.0

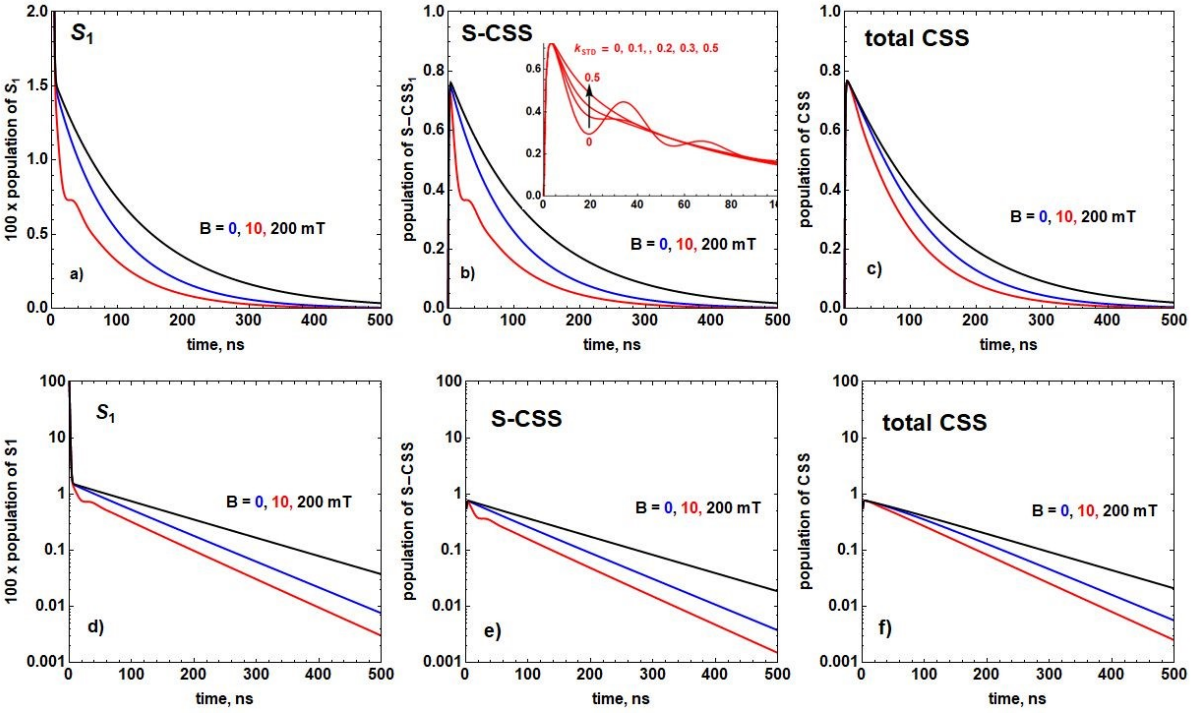

Fig. 4 Time evolution under conditions represented by the parameters in Table 2. Populations of S_1 (x 100) (a and d), S-CSS (b and e) in S_1-coupled CSS, total CSS (c and f) in S_1-coupled CSS at fields of 0 mT (blue), 10 mT (red) and 200 mT (black). Lower line: corresponding log plots. Inset in b) represents the curves at 10 mT for various values of k_{STD}. For comparison with the signals resultig in the case of absent kinetic coupling to S_1 cf. Supporting Information, section S3.

In Fig. 4, we represent the decays of S_1, the singlet part S-CSS of the CS-state, and the total CSS population as obtained quantum dynamically with the parameters in Table 2 for the S_1-CSS coupled system at zero field, the 2J-resonance field of 10 mT, and the effective high-field case at 200 mT. For the parameters chosen, a slight oscillating feature is still recognized for the singlet components S_1 and S-CSS. The oscillations clearly depend on the value of k_{STD}. For $k_{STD} = 0$ they are more pronounced than for $k_{STD} = 0.1$ in the standard parameter set, and they have disappeared for $k_{STD} = 0.5$ (cf. inset in Fig. 4b)).

In our case, the Fay and Manolopoulos[62] criterion for suppression of coherence in the S/T(±) transition at resonance (involving T+ for positive J and T− for negative J) can be written as

$$\gamma_{\mathrm{ST}_\pm} >> a/\sqrt{6} \approx 0.07 \qquad (33a)$$

with

$$\gamma_{\mathrm{ST}_\pm} = (k_S + k_{\mathrm{rCS}} + k_T)/2 + k_{STD} \qquad (33b)$$

For k_{STD} = 0 and the other parameter values given in Table 2, $\gamma_{\mathrm{ST}_\pm}$ is dominated by the large rate constants k_{T} and k_{rCS} and has a value of 0.023. This value is well below the threshold in Eq. (33a), indicating that coherence is not efficiently suppressed. In contrast, for k_{STD} = 0.5, $\gamma_{\mathrm{ST}_\pm}$ = 0.123, exceeding the threshold; accordingly, the oscillations are expected to disappear. This prediction is confirmed by the inset in Fig. 4b.

At zero field and in high field the energy gap between S and T is too large, and the amplitude of the oscillations too small for them to be observed in the decay signals. As follows from the log plots in Fig. 4, after the short initial stage the signals seem to decay exponentially. However, a closer look at the decay constants evaluated as a function of delay time (cf. Fig. 5) reveals that the instationary phase lasts about 200 ns, after which the decay rates become stationary. In Fig. 5a, this behaviour is demonstrated for the total population of the CS-state. Fig. 5b complements this information by showing that the relative populations of S_1 and the S-CS state become constant after about 200 ns, meaning that their decay rates are exctly the same as that of the total CSS population.

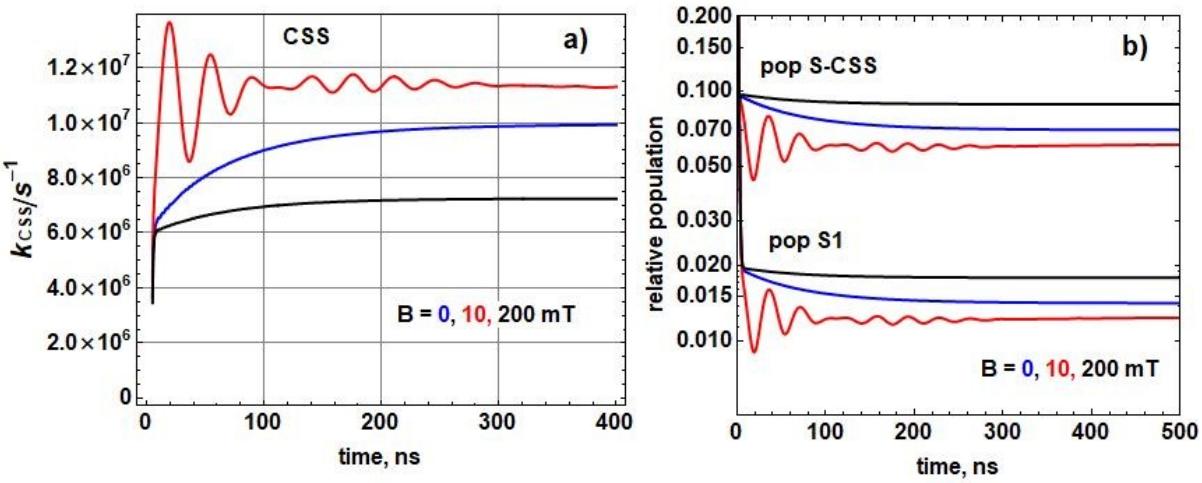

Fig. 5 a) Decay constant k_{CSS} (in absolute units) of the CS-state as function of delay time, calculated as the time derivative of the log of the CS-state population at 0, 10 and 200 mT. b) time dependence of fractional populations of S_1 and S-CS-state. (numerical calculation of the time derivation was not feasible in those cases, due to S/T_0 oscillations that, albeit of very small amplitude, lead to large variations of the slope).

The dependence of k_{slow} on the magnetic field is shown in Fig. 6. Several representative cases are considered. With neglect of relaxation (ΔA = 0) and without explicit S/T dephasing

View Article Online
DOI: 10.1039/D6CP00916F

(k_{STD}) (cf. Fig. 6a) the resonance appears relatively sharp and the base line outside the resonance is completely flat. The value of 0.006 (6×10^6 s^{-1}) corresponds to the sum of k_{slow} due to the kinetic coupling according to (32) plus k_S = 0.001 (10^6 s^{-1}) according to Table 2. Switching on of relaxation (cf. Fig. 6b) leads to an increase of k_{slow} at zero field because now relaxation allows for some admixture of T-CSS which decays faster (k_T = 0.025 (2.5×10^6 s^{-1})) than S-CSS. At the same time, the resonance broadens. On the high field side, k_{slow} deceases below the zero field value, because now the transitions S/T_+ and S/T_- are switched off due to the Zeeman splitting. Nevertheless the S/T_0 transition rate due to relaxation is high enough to populate enough T_0 as to yield much faster decay than without relaxation in case of Fig. 6a. Upon additional switching on of S/T dephasing (Fig. 6c) the broadening of the resonance increases.

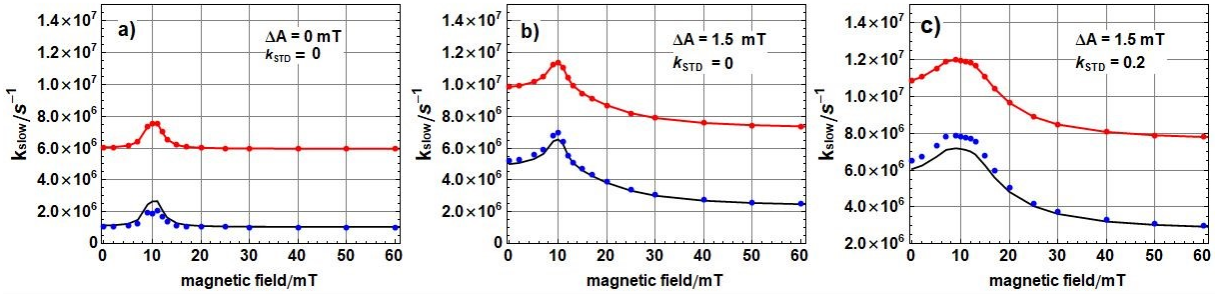

Fig. 6 Field dependence of k_{slow} for certain variations in the parameters. Red (solid line and datapoints): k_{slow} determined from exponential decay constant of total CSS population between 200 and 400 ns, calculated with full kinetic coupling to S_1. Blue, data points: quantum dynamically obtained decay constant $k_{CSS,qdwoS1}$ of CSS without kinetic coupling to S_1 but otherwise the same parameter values. Black, solid line: $k_{CSS,cl}$ value calculated by the classical model (eqn (32)). Except for the resonance region, the classical model yields very good predictions of the CSS-decay constant kinetically uncoupled from S_1 In a), the blue data points around 10 mT are problematic because the exponential decay approximation is poor. At earlier times, the actual decay constant for 10 mT is larger than at the neighbouring fields.

As shown in Fig. 3, the population of S_1, and thus the delayed fluorescence intensity, closely follows the population of the singlet component of the S-CSS, accurately reproducing its oscillation period, damping, and overall decay. On the other hand, Fig. S1 demonstrates that kinetic coupling between the CSS and S_1 modifies the decay behavior of the unperturbed CSS and further damps the oscillations, with the rate constants k_f,k_{CS} and k_{rCS} exerting distinct influences. These effects are analyzed and rationalized in detail in Section S4 of the Supporting Information. In addition to the features illustrated in Fig. 3, Fig. S5 highlights a further effect, namely a phase shift between the oscillations of the S_1 and S-CSS populations. This phase shift is governed primarily by the sum of the rate constants, k_{CS} + k_{rCS}.

View Article Online
DOI: 10.1039/D6CP00916F

In Fig. 6 are shown the rate constants $k_{CSS,qdwoS1}$ describing CSS decay, calculated quantum dynamically with the present parameter set but with the kinetic coupling to S_1 switched off. Relative to the corresponding k_{slow} values, these data points exhibit an approximately constant downward shift of 4.9×10^6 s^{-1}

The solid lines represent the rate constants $k_{CSS,cl}$ obtained by applying the classical model to the quantum-dynamical k_{slow} values calculated for the fully coupled S_1/CSS system. These values are obtained from Eq. (28), which follows from Eq. (25) by solving for k_{CSS} .

$$k_{CSS,cl} = \frac{k_f(k_{\mathrm{slow}}-k_{\mathrm{rCS}})+k_{\mathrm{CS}}k_{\mathrm{slow}}+k_{\mathrm{rCS}}k_{\mathrm{slow}}-k_{\mathrm{slow}}^2}{k_f+k_{\mathrm{CS}}-k_{slow}} \qquad (34)$$

Remarkably, although $k_{CSS,cl}$ is derived from the classical kinetic model of Scheme (24) using k_{slow} values obtained from a full quantum-dynamical calculation that includes the S_1 kinetics, the resulting "classical" values reproduce the quantum-dynamical rate constants $k_{CSS,qdwoS1}$ of the isolated CSS rather well. Significant deviations are observed only in the vicinity of the 2*J*- resonance, if the exponential approximation to the decay kinetics breaks down (cf. Fig. 6c).

The nearly field-independent parallel shift between the k_{slow} and $k_{CSS,cl}$ curves—and hence also, to a good approximation, between k_{slow} and the quantum-dynamical rate constants $k_{CSS,qdwoS1}$ of the uncoupled CSS—follows directly from Eq. (28):

$$k_{\mathrm{slow}} - k_{\mathrm{CSS,cl}} = \frac{k_{\mathrm{rCS}}(k_{\mathrm{f}}-k_{\mathrm{slow}})}{k_{\mathrm{CS}}+k_{\mathrm{f}}-k_{\mathrm{slow}}} \approx \frac{k_{\mathrm{rCS}}k_{\mathrm{f}}}{k_{\mathrm{CS}}+k_{\mathrm{f}}} \qquad (35)$$

where the final approximation is valid for $k_{slo} << k_f$, which is typically satisfied under the present conditions.

Conclusions

In this work, we have extended the spin-chemical description of hyperfine-coupled, rigidly linked radical pairs –typically realized as charge-separated states (CSS) in electron-donor-bridge-acceptor triads– to the case of reversible kinetic coupling with an electronically excited, fluorescing singlet state (S_1), which forms the basis of thermally activated delayed fluorescence (TADF). We have presented a systematic method for expanding the $(4\times n_N)$-dimensional electron-spin×nuclear-spin Hilbert space by an additional $(1\times n_N)$-dimensional S_1 × nuclear subspace. Compact expressions for the corresponding Liouville superoperators have been derived to account for S_1 decay and regeneration via fluorescence (k_f, including nonradiative decay), charge separation forming the singlet CSS (k_{CS}), reverse charge

View Article Online
DOI: 10.1039/D6CP00916F

separation regenerating S_1 (k_{rCS}), and the associated modifications of the CSS induced by reverse charge separation.

This formulation preserves full control over the nuclear-spin subspace during electronic transitions between S_1 and the CSS. Although hyperfine interactions are absent in S_1 and nuclear spin states are therefore conserved in this manifold, they continue to influence the overall spin dynamics in the CSS through the reversible kinetic exchange between S_1 and CSS. In this sense, the S_1 state acts as a shelving state for the nuclear spin degrees of freedom.

Numerical examples, ranging from minimal models to more realistic parameter sets, demonstrate that the present treatment provides a complete description of the sub-state information contained in the system. We show that the fluorescence signal from S_1 closely follows the population of the singlet CSS, including regimes exhibiting coherent oscillations. Comparison of the CSS dynamics under TADF conditions with those of a CSS not subject to reversible coupling to S_1 reveals an accelerated decay that is well described by the classical kinetic model (cf. eqn (32)). Although quantum beats in the unperturbed CSS are damped by reverse electron transfer at a rate determined by $k_{(}rCS_{)}$, they should remain observable under most realistic conditions.

These results establish a general theoretical framework for analyzing spin-dependent TADF and open new avenues for extracting radical-pair spin dynamics from time-resolved fluorescence measurements.

Data availability

The data supporting this article have been included as part of the ESI

Conflicts of Interest

There are no conflicts of interest to declare.

Acknowledgement

The author gratefully acknowledges the fruitful cooperation with Prof. Christoph Lambert and his group at the University of Würzburg and helpful discussion with Prof. Nikita Lukzen, International Tomography Center and Novosibirsk State University, Novosibirsk, Russia.

References

1. K. M. Salikhov, Y. N. Molin, R. Z. Sagdeev and A. L. Buchachenko, *Spin polarization and Magnetic Effects in Radical Reactions*, Elsevier, Amsterdam, the Netherlands, 1984.
2. K. M. Salikhov, *Bull. Russ. Acad. Sci.: Phys.*, 2025, **89**, 323 - 333.
3. U. E. Steiner and T. Ulrich, *Chem. Rev.*, 1989, **89**, 51 - 147.

4. U. E. Steiner and H. J. Wolff, in *Photochemistry and Photophysics*, eds. J. J. Rabek and G. W. Scott, CRC Press, Boca Raton, 1991, vol. IV, pp. 1-130.
5. S. Nagakura, H. Hayashi and T. Azumi, eds., *Dynamic Spin Chemistry. Magnetic Controls and Spin Dynamics of Chemical Reactions*, Kodansha and Wiley, Tokyo and New York, 1998.
6. P. J. Hore, K. L. Ivanov and M. R. Wasielewski, *J. chem. Phys.*, 2020, **152**, 120401.
7. A. M. Lewis, Spin Chemistry Community website, https://spin-chemistry-community.github.io/about/, (accessed 22.01., 2026).
8. R. W. Fessenden and R. H. Schuler, *J. Chem. Phys.*, 1963, **39**, 2147 - 2195.
9. B. Smaller, J. R. Remko and E. C. Avery, *J. Chem. Phys.*, 1968, **48**, 5174 - 5181.
10. R. Kaptein and J. L. Oosterhoff, *Chem. Phys. Lett.*, 1969, **4**, 195.
11. R. Kaptein and J. A. den Hollander, *J. Am. Chem. Soc.*, 1972, **94**, 6269-.
12. L. T. Muus, P. W. Atkins, K. A. McLauchlan and J. B. Pedersen, eds., *Chemically induced magnetic polarization, Proc. NATO Adv. Study Inst., Sogesto Urbino, Italy*, Reidel, Dordrecht, Holland, 1977.
13. R. Kaptein, in *Biological Magnetic Resonance: Volume 4*, eds. L. J. Berliner and J. Reuben, Springer US, Boston, MA, 1982, DOI: 10.1007/978-1-4615-6540-6_3, pp. 145-191.
14. M. Goez, in *Advances in Photochemistry*, eds. D. C. Neckers, D. H. Volman and G. von Bünau, Wiley, New York, 1997, vol. 23, pp. 63-163.
15. R. Z. Sagdeev, K. M. Salikhov, T. V. Leshina, M. A. Kamkha, S. M. Shein and Y. N. Molin, *J. Exp. Theor. Phys.*, 1972, **16**, 422-424.
16. K. M. Salikhov, F. S. Sarvarov, R. Z. Sagdeev, Y. N. Molin, T. V. Leshina, M. A. Kamkha and S. M. Shein, *Proceedings of XI European Congress on Molecular Spectroscopy, Tallin*, 1973, 363.
17. W. Lersch and M. E. Michel-Beyerle, *Chem. Phys.*, 1983, **78**, 115-126.
18. A. L. Buchachenko, *Russ. Chem. Rev.*, 1976, **45**, 761 -792.
19. E. L. Frankevich, A. I. Pristupa and V. I. Lesin, *Chem. Phys. Lett.*, 1977, **47**, 304-308.
20. B. Brocklehurst, *Chem. Phys. Lett.*, 1976, **44**, 245-248.
21. J. Klein and R. Voltz, *Phys. Rev. Lett.*, 1976, **36**, 1214-1217.
22. H. J. Werner, K. Schulten and A. Weller, *Biochimica et Biophysica Acta*, 1978, **502**, 255 - 256.
23. R. Haberkorn and M. E. Michel-Beyerle, *Biophys. J.*, 1979, **26**, 489-498.
24. A. J. Hoff, *Q. Rev. Biophys.*, 1981, **14**, 599-665.
25. K. Schulten, C. E. Swenberg and A. Weller, *Z. Physik. Chem. N. F.*, 1978, **111**, 1-5.
26. K. Maeda, H. K. B., F. Cintolesi, I. Kuprov, C. T. Rodgers, P. A. Lidell, D. Gust, C. R. Timmel and P. J. Hore, *Nature*, 2008, **453**, 387-390.
27. M. Tiersch and H. J. Briegel, *Phil. Trans. R. Soc. Lond. A*, 2012, **370**, 4517-4541.
28. I. A. Solov'yov, T. Ritz, K. Schulten and P. J. Hore, in *Quantum effects in biology*, eds. M. Mohseni, Y. Omar, G. Engel and M. B. Plenio, Cambridge University Press, Cambridge, UK, 2014.
29. H. G. Hiscock, S. Bourne Worster, D. R. Kattnig, C. Steers, Y. Jin, D. E. Manolopoulos, H. Mouritsen and P. J. Hore, *PNAS*, 2016, **113**, 4636-4639.
30. T. P. Fay, L. P. Lindoy, D. E. Manolopoulos and P. J. Hore, *Faraday Discuss.*, 2020, **221**, 77-91.
31. H. Hayashi and S. Nagakura, *Bull. Chem. Soc. Jap.*, 1984, **57**, 322-328.
32. J. H. Klein, D. Schmidt, U. E. Steiner and C. Lambert, *J. Am. Chem. Soc.*, 2015, **137**, 11011-11021.
33. M. R. Wasielewski, M. D. E. Forbes, N. L. Frank, K. Kowalski, G. D. Scholes, J. Yuen-Zhou, M. A. Baldo, D. E. Freedman, R. H. Goldsmith, T. Goodson, M. L. Kirk, J. K. McCusker, J. P. Ogilvie, D. A. Shultz, S. Stoll and K. B. Whaley, *Nat. Rev. Chem.*, 2020, **4**, 490-504.
34. P. Gilch, F. Pöllinger-Dammer, C. Musewald, U. E. Steiner and M. E. Michel-Beyerle, *Science*, 1998, **281**, 982 - 984.
35. M. Liu, J. Zhu, G. Zhao, Y. Li, Y. Yang, K. Gao and K. Wu, *Nature Materials*, 2025, **24**, 260-267.

View Article Online
DOI: 10.1039/D6CP00916F

36. G. Kothe, S. Weber, E. Ohmes, M. C. Thurnauer and J. R. Norris, *J. Am. Chem. Soc.*, 1994, **116**, 7729-7734.
37. S. Weber, E. Ohmes, M. C. Thurnauer, J. R. Norris and G. Kothe, *Proc. Natl. Acad. Sci.*, 1995, **92**, 7789-7793.
38. D. Mims, J. Herpich, N. N. Lukzen, U. E. Steiner and C. Lambert, *Science*, 2021, **374**, 1470-1474.
39. B. Brocklehurst, *Radiat.Phys.Chem.*, 1997, **50**, 213-225.
40. O. A. Anisimov, V. L. Bizyaev, N. N. Lukzen, V. M. Grigoryants and Y. N. Molin, *Chem. Phys. Lett.*, 1983, **101**, 131-135.
41. A. Weller, *Z. Physik. Chem. N. F.*, 1982, **133**, 93-98.
42. H. Staerk, W. Kühnle, R. Treichel and A. Weller, *Chem. Phys. Lett.*, 1985, **118**, 19-24.
43. M. Chowdhury, R. Dutta, S. Basu and D. Nath, *Journal of Molecular Liquids*, 1993, **57**, 195-228.
44. D. R. Kattnig, A. Rosspeintner and G. Grampp, *Angew. Chem. Int. Ed.*, 2008, **47**, 960.
45. S. Richert, A. Rosspeintner, S. Landgraf, G. Grampp, E. Vauthey and D. R. Kattnig, *J. Am. Chem. Soc.*, 2013, **135**, 15144-15152.
46. J. T. Buck and T. Mani, *J. Am. Chem. Soc.*, 2020, **142**, 20691 - 20700.
47. N. LIn, M. Tsuji, I. Bruzzese, A. Chen, M. Vrionides, N. Jian, F. Kittur, T. P. Fay and T. Mani, *J. Am. Chem. Soc.*, 2025, **147**, 11062–11071.
48. T. Groß, M. Holzapfel, A. Schmiedel, B. Woodward, U. E. Steiner and C. Lambert, *Chemical Science*, 2026, **submitted**.
49. K. Maeda, A. J. Robinson, K. B. Henbest, H. J. Hogben, T. Biskup, M. Ahmad, E. Schleicher, S. Weber, C. R. Timmel and P. J. Hore, *PNAS*, 2012, **109**, 4774-4779.
50. T. P. Fay, L. P. Lindoy and D. E. Manolopoulos, *J. Chem. Phys.*, 2019, **151**, 154117.
51. J. Schäfer, M. Holzapfel, A. Schmiedel, U. E. Steiner and C. Lambert, *Physical Chemistry Chemical Physics*, 2018, **20**, 27093.
52. U. E. Steiner, J. Schäfer, N. N. Lukzen and C. Lambert, *Journal of Physical Chemistry C*, 2018, **122**, 11701-11708.
53. D. Mims, A. Schmiedel, M. Holzapfel, N. N. Lukzen, C. Lambert and U. E. Steiner, *J. Chem. Phys.*, 2019, **151**, 244308.
54. S. Riese, L. Mungenast, A. Schmiedel, M. Holzapfel, N. N. Lukzen, U. E. Steiner and C. Lambert, *Mol. Phys.*, 2019, **117**, 2632-2644.
55. C. Lambert, C. Roger, A. Schmiedel, M. Holzapfel, N. Lukzen and U. E. Steiner, *Physical Chemistry Chemical Physics*, 2024, **26**, 24983-24994.
56. C. Roger, A. Schmiedel, M. Holzapfel, N. N. Lukzen, U. E. Steiner and C. Lambert, *Physical Chemistry Chemical Physics*, 2024, **26**, 4954-4967.
57. P. Mentzel, L. Gerhards, D. Koppenhöfer, A. Schmiedel, M. Holzapfel, N. Lukzen Nikita, A. Solov'yov Ilia, U. E. Steiner and C. Lambert, *J. Am. Chem. Soc.*, 2025, **147**, 23968-23078.
58. R. Haberkorn, *Mol. Phys.*, 1976, **32**, 1491-1493.
59. N. N. Lukzen, J. H. Klein, C. Lambert and U. E. Steiner, *Z. Physik. Chem. N. F.*, 2017, **231**, 197-223.
60. T. P. Fay, L. P. Lindoy and D. E. Manolopoulos, *The Journal of Chemical Physics*, 2018, **149**, 064107.
61. J. A. Jones and P. J. Hore, *Chem. Phys. Lett.*, 2010, **488**, 90–93.
62. T. P. Fay and D. E. Manolopoulos, *J. Chem. Phys.*, 2019, **150**, 151102.

View Article Online
DOI: 10.1039/D6CP00916F

Data Availability Statement

The data supporting this article have been included in the main manuscript and as part of the Supplementary Information.